UNIVERSITÀ
DEGLI STUDI
DI PADOVA

UNIVERSITY OF PADOVA

Department of Industrial Engineering DII

MSc Course in Aerospace Engineering

Impact of vaneless diffuser geometry on stall mechanism development

Supervisor Prof. Benini Ernesto

Co-Supervisor Prof. Binder Nicolas

Jacopo La Gamba – 2095565

Academic Year 2023/2024

Contents

Abstract

This research is intended to provide a better understanding on the impact of geometry on stall mechanism and stall development within vaneless diffuser of centrifugal compressors. Evaluating the critical angle for stall and confronting the trend for different geometries.
The study is confined to the diffuser only, which mesh has been tested and validated in previous work. A full annulus simulation was carried out.
The analysis was conducted with the use of Computational Fluid Dynamics, or CFD, on the software StarCCM. The numerical set-up employed unsteady RANS simulation and SST $k-\omega$ turbulence model.
In particular, starting from the parallel wall geometry, after comparing the obtained results with literature ones, other three different geometries, evolved from the former one, were investigated, gradually modifying the angle of divergence at the shroud.
These new divergent diffusers were analyzed to figure out whether their stall behavior was similar to the initial case.
The results obtained from CFD were then post-processed through Matlab and spatial Fourier analysis was involved. This was necessary to objectively point out the critical angles. The Fourier analysis enabled the dominant frequencies highlight.
Successively, a performance analysis was executed to better understand losses evolution in the geometries and to observe the mass flow trend as well.
The work focused on flow field examination, to clarify a conceivable physical interpretation for the noted radial velocity fluctuations and the stall mechanism feature among different geometries.

Abstract

Questa ricerca intende fornire una migliore comprensione dell'impatto della geometria sul meccanismo di stallo e sullo sviluppo dello stallo all'interno dei diffusori vaneless dei compressori centrifughi. Valutando l'angolo critico per lo stallo e confrontando l'andamento per diverse geometrie.
Lo studio si limita al solo diffusore, la cui mesh è stata testata e convalidata in precedenti lavori. È stata effettuata una simulazione sull'intero anello. L'analisi è stata condotta con l'ausilio della fluidodinamica computazionale, o CFD, con il software StarCCM. Il set-up numerico ha impiegato simulazioni RANS non stazionarie ed il modello di turbolenza SST $k-\omega$.
In particolare, a partire dalla geometria a pareti parallele, dopo aver confrontato i risultati ottenuti con quelli già presenti in letteratura, sono state adottate altre tre diverse geometrie, derivanti dalla prima, sono state studiate, modificando gradualmente l'angolo di divergenza della parete superiore. Questi nuovi diffusori divergenti sono stati analizzati per capire se l'evoluzione dello stallo fosse simile al caso iniziale. I risultati ottenuti dalla CFD sono stati poi analizzati tramite Matlab e si è proceduto all'analisi spaziale tramite trasformate di Fourier. Questo è stato necessario per evidenziare in modo oggetto gli angoli critici. L'analisi di Fourier ha permesso di evidenziare le frequenze dominanti.
Successivamente, è stata eseguita un'analisi delle prestazioni per comprendere meglio l'evoluzione delle perdite nelle varie geometrie ed osservare l'andamento della portata di massa.
Il lavoro si è concentrato sull'esame del campo di flusso, per chiarire una possibile interpretazione fisica delle fluttuazioni di velocità radiali osservate e del meccanismo di stallo tra le diverse geometrie.

1 Introduction

In the wide aerospace field and in the wider industrial environment, there is a subsystem that is crucial: turbomachinery.
The field of turbomachinery encompasses the study, design, analysis, and optimization of various types of rotating machinery that deal with the fluids. These machines are primarily used for the conversion of energy between mechanical work and fluid flow. Such machines are composed of different parts, the main is the compressor.
A compressor is an object able to absorb energy in order to produce work on the fluid, this ability enables the increment of pressure and, subsequently, the increase of temperature in the flow. Similar to other machines, compressors exhibit their own characteristic and stability range, with peculiar working conditions, limited by the stability criteria that are fundamental for their efficiency and reliability.
Centrifugal compressors have been used in aviation industry, especially during the beginning of the flight world, replacing the internal combustion engines. They were employed for the firs two jet engines, in 1935-1940. Despite actual aircraft engines are fitted, for the majority, with axial design because of its simplicity, centrifugal compressors are still used in some branches of the aerospace environment. For instance:

- Aircraft Auxiliary Power Unit (often referred to as APU)
- Helicopter engines (e.g. Kamax K-MAX)
- Aircraft systems (De-icing, Fuel, Hydraulics)

This research has the scope of investigating whether is possible or not extend the range operativity of centrifugal compressor, with particular focus on the key role played by the diffuser, a subcomponent of the system. It is needed to slow down the flow at the impeller outlet, meanwhile increasing the pressure, so it convert kinetic energy into enthalpy. During the last century, efforts have been made by the industry to provide an extension of the working conditions. Although noticeable progresses were made, the majority of the research focused on the impeller range, providing excellent results.
More endeavours should be made on the other components, in particular extending the diffuser operativity could provide, at least, 3 important benefits. For example:

- General performance optimization
- Energy saving and pressure recovery
- Enhanced reliability

This thesis aims to evaluate whether the pressure recovery and leakage decrease can justify the geometry change for vaneless diffusers. The limitation due to stall phenomena in particular are dealt with, surge and stall cells formation mechanism are examined as well. The analysis is carried out with computational fluid dynamics (CFD).
The thesis will be structured as follows: in the first part, chapter 2 and 3 respectively, a short introduction to centrifugal compressors and a brief overview of diffusers and their role are provided; the 4^{th} chapter introduces the work and the related challenges; in the following chapter, 5, the results are presented in every details; chapter 6 is devoted to discuss possible future projects and conclusions.

2 Centrifugal compressors

In turbomachinery, compressors can be divided into two groups: axial and centrifugal. This division is due to the fact that the former category has an axial distribution of the flow, while the second one has a radial configuration. In modern aircraft the axial compressors are preferred due to their capacity of elaborating high mass flow rate and their assembly simplicity. Nevertheless, centrifugal compressors have been used firstly and they are still being used in different applications, as explained in the introduction.
These type of compressors have some advantages over axial ones, for example their behaviour in off-design conditions is better and their performance range is wider. In ground power plants the centrifugal compressor is preferred over the axial due to the higher single stage pressure ratio that can be achieved, thus greater density power.

2.1 Stage dynamics and basic principles

In the first section of the rotor, known as the inducer, the flow usually enters following the axial direction, leaving this section without any axial component. The whole rotor section is called the impeller. The impeller imparts energy due to its curved and twisted aerodynamic surfaces, the blades.
The flow is decelerated outward, according to Bernoulli equation the flow will increase its pressure, as expected for a compressor. The pressure rise is achieved through large radial shift between inlet and outlet of the impeller. This involves the reduction of the frontal area by design, thus a smaller mass flow rate than axial compressors.
Usually the velocity triangles are employed to explain the relationship between the three components of the velocity and their changes in the rotor. In particular, the velocities are: absolute velocity c; relative velocity w; tangential blade speed U. Where the last one can be evaluated as $U = \omega \cdot r$. The velocity equation is:

$$\vec{c} = \vec{w} + \vec{U}$$

For instance, in a centrifugal compressor the following $U_2 > U_1$ is always true. Hence, if the design for the relative velocity is chosen to be $w_2 = w_1$, then the absolute velocity have to satisfy $c_2 > c_1$, as shown in the figure 1.

It is important to highlight that the two triangles lie in two different planes from the inlet to the outlet.
The impeller outlet has the key role of turning the flow in the radial direction, meanwhile accelerating the fluid in the tangential direction. The change of the angular momentum is caused by the torque on the fluid, thus can be evaluated as:

$$\tau_{fluid} = \dot{m} \cdot (r_2 \cdot c_{\theta 2} - r_1 \cdot c_{\theta 1}) = -\tau_{blade}$$

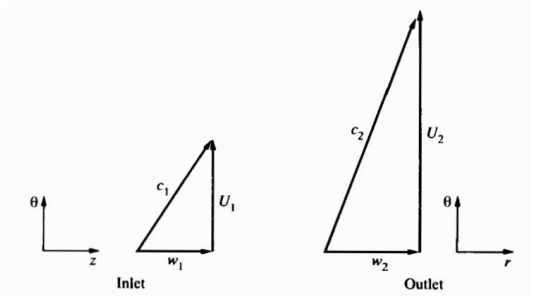

Figure 1: Velocities triangles [1]

Since the radius at the outlet, r_2, is greater than the inlet one, the torque acting on the fluid is positive and the torque on the blade is negative, therefore the compressor has to perform work, consistently with the convention in the first law of thermodynamics.
In a centrifugal compressor a transonic or supersonic velocity at the outlet of the impeller is often achieved. Thus, in order to reduce the speed and increase the pressure, a diffuser is located at the outlet.
The flow is then collected in a volute, since it is necessary to reset the axial condition for either the subsequent stage or the combustion chamber.

2.2 Performance

A performance map, or curve, is a valid instrument for describing the compressor by non-dimensional numbers. Generally group of parameters can be associated to a dimensionless quantity, such as the Reynolds number. It is represented as a chart, usually the pressure ratio and the isentropic efficiency are shown as function of the mass flow rate and the rotational speed. In particular it can be stated that:

$$\frac{p_{03}}{p_{01}}, \eta_c = f\left(\frac{\dot{m}\sqrt{\theta}}{\delta}, \frac{N}{\sqrt{\theta}}\right)$$

Attention must be taken using consistent units of measure. This equation is derived from the Buckingham theorem, that states: the number of dimensionless groups can be determined by n - m = k, where n is the number of variables, m is the number of fundamental dimensions, and k is the number of dimensionless groups.

The map shows the pressure ratio as a function of the mass flow, firstly there are two different lines that encompass the whole region: surge line and choke line. The surge is an off-design condition, it is the technical compressor limit. The surge is a 3D phenomenon that involves the complete compressor, this may

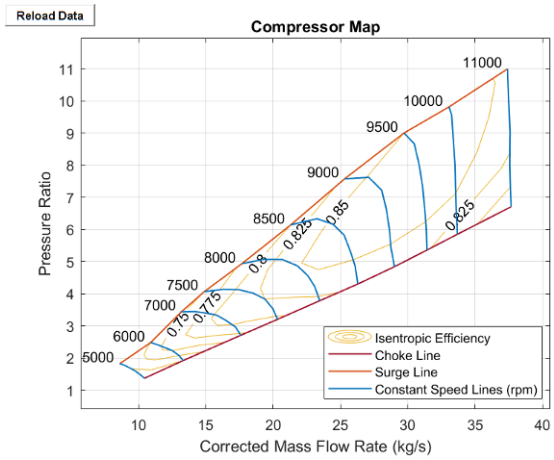

Figure 2: Typical performance map [1]

lead to violent fluid oscillations and time dependent forces, compromising the machine.
The choke is the other off-design condition, in this case it is due to the velocity reaching a sonic condition in some point within the rotor stage. Thus, the compressor can not elaborate further mass flow rate. The lines that reach the choke line are called iso-velocity lines, they represent a given operating condition for the speed of the compressor. It worth to point out how the slope of the line is getting vertical along the increase of the rotational speed, this is being caused by the aerodynamic instabilities.
The isentropic efficiency is the second feature of the map, shown by the iso-efficiency curves, each curve shows the efficiency of the compressor in the enclosed area.

2.3 Compressor configurations

Depending on the context, centrifugal compressor can have various configurations. The inducer is often mounted on compressor because it reduces the possibility of flow separation, limiting also the maximum turn the flow can experience. Some centrifugal compressors are crafted without the inducer, this result in a very noisy machine, due to the boundary layer separation. For example, small centrifugal blower for air conditioning may not require an inducer, therefore reducing costs for manufacturing.
The blades in the impeller can be ranked upon their exit blade angle, namely β_2. In particular there are three geometries:

- Radial impeller
- Forward-leaning impeller
- Backward-leaning impeller (or backswept impeller)

The first design is quite used due to less structural problems, since the blade angle is equal to 90 degrees. The efficiency of this configuration is high and the losses are acceptable, however according to Euler equation the pressure rise will proportionally to the wheel speed and the maximum speed is not achievable with this configuration.
Forward-leaning is often employed in high-power machines, at the impeller outlet the reached Mach number is the highest of all three cases, hence the poor pressure recovery and efficiency in the radial diffuser. In addition, the structural loading acting on the blades is critical, attention must be taken in optimising the curvature, otherwise the structure could not match the loads.
The last configuration consists in blades curved in the same direction as the rotation of the impeller. This is typical of fan or blower, since this design has the lowest mach number at the exit among the three, high efficiency diffusion can be achieved. The drawbacks, as in the previous case, are the structural loads acting on the blade.

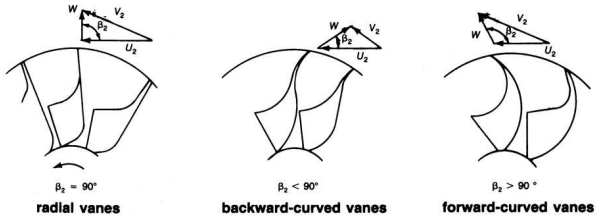

Figure 3: Types of impeller [1]

2.4 Compressor design

The compression process within the compressor should be optimized to achieve maximum efficiency, hence minimizing the mechanical energy required from the shaft. Resulting in improved overall performance and reduced energy consumption. The isentropic efficiency serves as the parameter that characterizes this phenomenon. In particular, the parameter, namely η, considers only the thermodynamic perspective of the compression. Therefore, it is not sufficient to analyze and to describe machines that have different operating points, due to pressure ratio dependency. The coefficient can be evaluated as:

$$\eta_{\text{is}} = \frac{\text{Actual work done on the fluid}}{\text{Work done on the fluid under adiabatic conditions}} = \frac{h_{03_s} - h_{01}}{h_{03} - h_{01}}$$

Whereas if the pressure ratio is made explicit, the formula can be recasted as:

$$\eta_{\text{is}} = \frac{\pi^{\frac{\gamma-1}{\gamma}} - 1}{\frac{T_3}{T_1} - 1}$$

As aforementioned, this coefficient, by definition, is not accurate enough. As a matter of fact, the η_{is} will decrease as the outlet temperature will increase, this is explained noting the isotherms divergence on the thermodynamic chart or Mollier diagram.
Thus, polytropic efficiency is generally employed. The definition of this coefficient, η_{pol}, is not based on the pressure ratio, is defined as the isentropic efficiency of a thermodynamic adiabatic process in which the initial and final pressure present an infinitesimal difference.
Polytropic efficiency is defined by:

$$\eta_{\text{pol}} = \frac{dh_{is}}{dh}$$

Since the polytropic efficiency is set, the final formula can be displayed as:

$$\eta_{\text{pol}} = \frac{\gamma - 1}{\gamma} \frac{ln\frac{p_2^0}{p_1^0}}{ln\frac{T_2^0}{T_1^0}}$$

The definition of this parameter can be visualized in figure 4.

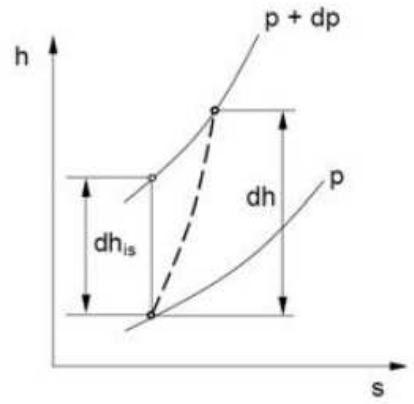

Figure 4: Visualization of the polytropic efficiency [1]

For a centrifugal compressor the polytropic efficiency can be plotted as a function of the isentropic efficiency, the link between the two is shown in figure 5.
It is worth noting that in every circumstances, if the pressure ratio will increase, the polytropic efficiency will decrease. At the same pressure ratio conditions, the drop experienced by η_{pol} will be greater for compressor with lower η_{is} (i.e. if the quality of the compressor design is low).

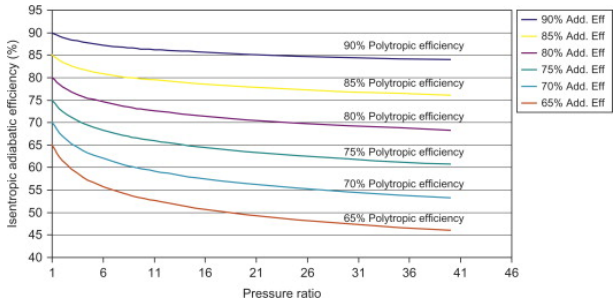

Figure 5: Relationship between polytropic and isentropic efficiency [1]

2.5 Methods to enhance performance

Enhancing performance of compressors has always been a challenge, even more so in the last twenty years due climate change and environmental issues. Thanks to the computational fluid dynamics (CFD), the analysis were improved and have been easier since then, relying on new equipment with enormous computing abilities.

The optimization can be performed on every sub-component of the compressor, starting from the inudcer. For instance, the pre-swirl rotation, obtained via the Inlet Guide Vanes (IGV) as an effect on the flow field and the whole machine. Both mass flow and pressure ratio decrease with positive pre-rotation, but the margin of stability is increased, hence it is a valuable trade-off. However, flow control methods were researched in literature, to minimize the losses and improve efficiency, with a three-dimensional Reynolds Averaged Navier-Stokes simulations. [2]

Genetics algorithm and CFD analysis can be used together to optimize the design of the impeller, developing a complete 3D model and be able to investigate the changes in different parameters, such as the blade angle or the starting point of splitter blades. [3]

The structure itself can be modified, the impeller is realized either with or without the shroud and this affect the limiting range operativity in terms of maximum tangential blade speed. To improve the stall margin, despite a reduction in isentropic efficiency, it was investigated the possibility of case treatment. [4]

In this work, the analysis will focus on vaneless diffusers and their design.

3 Diffuser

The flow leaving the impeller enters a radial diffuser. As a matter of fact, the flow is highly non-uniform, there are axial and circumferential distortion at the inlet, thus velocity variations in both magnitude and direction are experienced in the diffuser.
At the impeller outlet the flow is characterized by swirl and the streamlines can be represented by spirals. The diffuser can be divided into two sections: vaneless and vaned. The design is influenced by various parameters, such as Mach number and pressure rise.
Due to the absence of a choke point that could restrict flow under heavy load, a vaneless diffuser boasts a wider operational spectrum compared to a vaned diffuser of similar dimensions. Consequently, vaneless diffusers find extensive application in process compressors and turbochargers, especially in scenarios with notable variations in mass flow rates arising from different modes of operation.

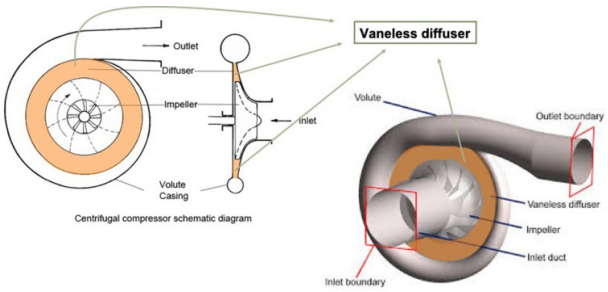

Figure 6: 3D view of a generic vaneless diffuser [19]

The correct matching between impeller and diffuser is crucial to maximize the efficiency of the compressor, avoiding decreases in the pressure ratio and mass flow rate. [9]

3.1 Working principle

Initially, the flow is considered incompressible, the continuity equation must be satisfied for a general diffuser with parallel walls, width h:

$$rc_\theta = constant$$

Where the mass flow rate can be evaluated as:

$$\dot{m} = \rho A c_r = \rho(2\pi h r)c_r$$

The first equation states that the circumferential velocity of the flow should

decrease, since the increase of the radius diffuser.
If the torque due to wall friction is neglected, then the continuity equation requires the conservation of angular momentum through the vaneless region cross sectional area, thus:

$$rc_\theta = constant$$

If velocity equations are combined, then it can be shown that:

$$\frac{c_\theta}{c_r} = constant = \tan\alpha$$

The actual flow is compressible, hence the equations depends on Mach number, however they can be simplified by assuming the flow reversible. To avoid overloading the subject, the final result is just shown, for a in-depth discussion refer to [10].

$$\frac{\tan\alpha^*}{\tan\alpha} = \frac{\rho^*}{\rho} = \left(\frac{1+\frac{\gamma-1}{2}M^2}{1+\frac{\gamma-1}{2}}\right)^{\frac{1}{\gamma-1}}$$

Where ρ^* is the characteristic density and α^* is the characteristic angle; these values are based on initial inlet conditions.
Generally, the flow leaving the impeller has two regions. The jet-wake phenomenon enables the mixing zone to be reduced respect with a steady parallel flow. This happens because of the unsteady change in both magnitude and direction of the jet and wake velocities, therefore the result is an intense transfer of energy, aided by wall friction. The large total pressure loss is a secondary effect of the same mixing mechanism.

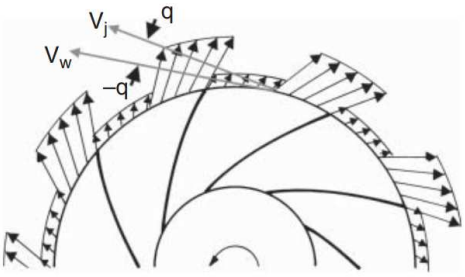

Figure 7: Illustration of jet and wake zone at impeller exit [1]

As the flow progresses downstream within the diffuser, the total pressure gradient becomes a key factor, leading to a rise in radial velocity. Thus, the flow

becomes concentrated on the side with the highest total pressure.
It was demonstrated [12] that the concentration of the flow on one side of the diffuser may enable flow recirculation on the opposite side (i.e. backflow). This is the baseline for the development of stall cells and subsequently abrupt stall (or surge).
The vaneless diffuser can provide the deceleration of the flow and the increase in the pressure, however this might result in a high outer radius value. This property reduces the feasibility of large vaneless diffuser, particularly in aircraft applications, where the engine dimension is a design driver in most cases. Whether the application do not have a constraint on dimension, the otulet radius can be increased, but generally the ratio between the radii is kept under 2, since there is not a effective improvement on the performance. [11]
Another important feature of the vaneless diffuser is the suitability in off-design conditions, hence a wider operativity range.

3.2 Key parameters

To analyze a general diffuser, as others turbomachinery components, non dimensional parameters are generally employed. As a matter of fact, the widespread decision of using dimensionless metrics is due to the possibility of comparing and confronting different machines in terms of size, power or volume. For instance, the different geometric configurations may be compared through the use of two parameters.
The following features have been chosen for this analysis:

$$\text{Static pressure recovery} \qquad C_p = \frac{P_s^{out} - P_s^{in}}{P_t^{in} - P_s^{in}}$$

and

$$\text{Total pressure loss} \qquad \eta = \frac{P_t^{in} - P_t^{out}}{P_t^{in} - P_s^{in}}$$

according to the formalism used by Turunen-Saaresti. [13]
The superscript *in* and *out* refer to the pressure measured at the inlet and the outlet, respectively. While the subscript s and t refer to the static or total pressure, respectively.
The difference between total pressure and static pressure is briefly outlined hereby.
Static pressure represents the pressure that would be measured by a pressure sensor placed in the fluid stream without affecting the flow, it is a component of the total pressure.
Total pressure represents the maximum pressure that a fluid could exert if brought to rest adiabatically and isentropically. Can be also indicated as stagnation pressure, it is the sum of static pressure and dynamic pressure. It is worth highlighting that in the general case of viscous, compressible flow, as in this scenario, Bernoulli equation is not valid.

3.3 Stall

Various articles have been written and many researchers have endeavored to indicate the pattern of stall mechanism in the diffuser. Although general knowledge about diffuser increased in the past century, a formal answer has yet to be found. [14]
To better comprehend the stall mechanism, a distinction must be made about stall and surge, these terms are often used as synonyms, but they have different meanings. The stall is a 1D phenomenon, it can occurs in any section of the diffuser (or every other component), it is enabled by boundary layer separation and backflow vortices, this results in overall performance decrease. While the surge is a 3D phenomenon that involves the whole machine, thus making the machine unable to work.
Outstanding results have been found in vaneless diffuser since the simplicity of the design and the geometry allowed to modelling of the flow structure in a precise fashion. According to Fujisawa [15], the gradient of the pressure along the span, induces the flow concentration on the side in which the pressure higher. After separation, the generation of pressure gradient inversion occurs, this variation persist until the flow reversal takes place on the opposite side. Thus, the separation starts occurring at both hub and shroud side.
Practically, it can be observed that the flow starts to pulse, showing high non-uniformity with the channel that is subjected to boundary layer separation in different points. At this time the flow field is unstable and behaves in a wave manner, oscillating and hitting hub and shroud spots, thus increasing the turbulence in the diffuser.

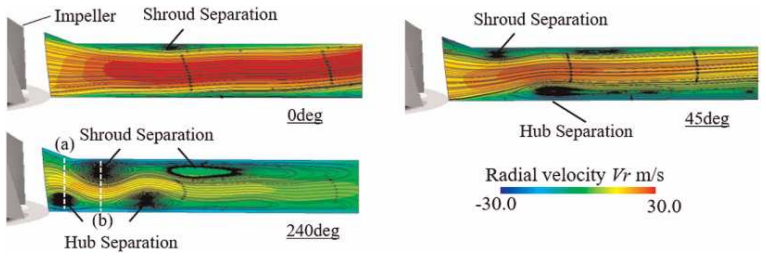

Figure 8: Fluid behaviour near stall condition, reproduced from [15]

One of the two most accepted theories on rotating stall is attributed to Senoo and Kenoshita [16], providing important information about boundary layer behaviour, the analysis carried out claimed that the rotating stall mechanism is strongly influenced by the three-dimensional distortion boundary layer.
The behaviour and the differences between theories can be explained as follow: the structure of the flow and, moreover, the structure of the boundary layer depend on diffuser's geometry. Thus, according to Ljevar et Al [17], in narrow diffuser the most important phenomenon is the merge of boundary layer, then lately the rotating stall is formed. In wide diffuser, the core flow, due to its

own stability, increases the general stability of the component, therefore the reason linked to the stall is the core flow stability rather than the boundary layer behaviour.

3.4 Geometric configurations

The geometry of the diffuser has a crucial impact on both performance and stall mechanism. Moreover a priori it can not be stated what kind of stall will arise in the diffuser. Although the literature presents multiple cases about rotating stall in vaneless diffuser with parallel wall, the pattern that developes in different geometries is still not completely defined. Nonetheless, there exists articles comparing such differences, for example convergent diffusers with standard ones, by Zhang et Al. [18]. In the mentioned paper, only the convergent geometry was analyzed, modifying either the wall at the shroud or at the hub.
In this work, the general case with parallel wall diffuser is addressed, then divergent wall case is dealt with. Precisely, three cases were developed with different divergent angles for the shroud wall, while the hub wall remained straight.
To compare different geometries, it has to be imposed the same grade of diffusion for a fixed angle. Thus, diffuser's outlet passage areas must be the same. If the divergence angle is referred to as θ_D, the outlet radii for parallel wall case and divergent wall case are indicated, respectively, as: R_P^{out} and R_D^{out}. Then the outlet radius for the divergent case can be evaluated from the following equation:

$$R_D^{out} = \frac{1}{2} \cdot \left(R_P^{in} - \frac{h}{2\tan(\theta_D)} + \sqrt{\left(\frac{h}{2\tan(\theta_D)} - R_D^{in} \right)^2 + \frac{2h \cdot R_P^{out}}{\tan(\theta_D)}} \right)$$

Thus there is an inverse proportion between R_D^{out} and θ_D. As expected, if the divergence angle increases, the radius reduces, in order to maintain the area constant.

4 Experimental work

The scope of this work is to understand stall mechanism in vaneless diffusers of centrifugal compressor. Stall is an extremely complex phenomenon in which boundary layer separation and backflow vortices take part. To observe this phenomena the CFD is crucial. Therefore, the work relies on observation of flow field through StarCCM software and frequency analysis.
As briefly discussed in the previous chapter, the stall development in parallel wall vaneless diffuser has been deeply studied, while the behaviour of the flow in proximity of the stall in divergent vaneless diffusers is not fully understood. The experiment has as objective to detect the critical angle for which the stall is firstly developed. To determine exactly the correct angle is used an impartial method, based on fast Fourier transform analysis. Furthermore, the second goal of this experiment is to discuss the mechanism of stall development, with regard to the different geometries.

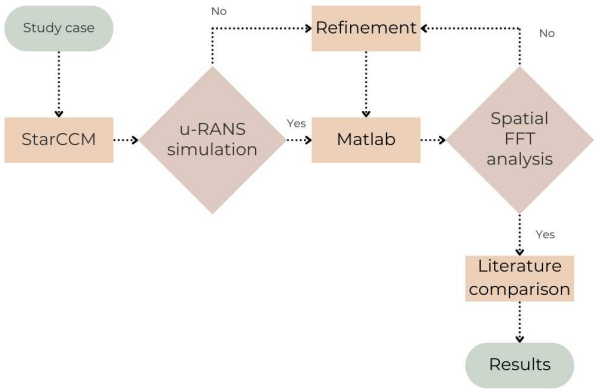

Figure 9: Flowchart of the work

4.1 Numerical model

Nowadays the majority of the experiments make use of Computational Fluid Dynamics (CFD), that enables studies that would require the full analysis of Navier-Stokes equations. The CFD, however, can not provide unlimited resources, even though it enhanced the ease to tackle complex problems. Therefore the variables must be minimized to reduce the computer work, in particular some assumptions regarding flow condition (e.g. compressible flow) should be done.
Moreover, the Navier-Stokes equations can be interpreted differently according to the method that is used to represent them and that is used to simulate the problem. In particular, there are three ways of modelling the flow field using CFD:

- Direct Numerical Simulation - DNS
- Reynolds Average Numerical Simulation - RANS
- Large Eddy Simulation - LES

In this case, RANS are used, since they are a good trade-off between time and accuracy model. In fact, the RANS are generally used in experiments which do not require particular description of the smallest scale of the flow. Instead, when the flow is turbulent and the smaller eddies need to be described DNS and LES are employed. Obviously every model has it own advantages and disadvantages. In particular, RANS does not display the smallest structures of the flow field, but are useful to simulate the impact of turbulence on mean values, reducing the computational work.

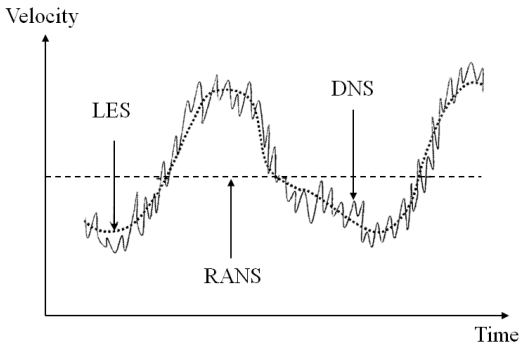

Figure 10: Differences between DNS, LES, RANS [6]

The fundamental part of the RANS is the decomposition of a generic quantity (e.g. the velocity) into a time averaged component (mean value) and a time dependent fluctuation:

$$u = \bar{u} + u'$$

Since the fluid is compressible, the density variation has to be taken into account, therefore it is introduced a density-weighted average model (also known as Favre averaging) that brings to:

$$u = \tilde{u} + u''$$

To avoid weighing down the discussion, the complete Reynolds Average Navier-Stokes equation are not displayed here, but a formal description can be found in [5].
The most important feature coming from these new equations is the Reynolds

Stress Tensor, that is a rank 2 tensor, with 6 new unknowns. The most important closure model is given by Bousinessq hypothesis, introducing therefore the concept of eddy viscosity. Although this hypothesis is accurate for flows that show well-defined shear layers, for different cases more precise models have been developed and are actually used.
The SST $k-\omega$ Turbulence Model is used for this work. It is a model proposed by Menter, this model combines two different equations for eddy viscosity, so called $k-\omega$ and $K-\epsilon$. The SST (Shear Stress Transport) model employ the $k-\omega$ for the inner region (or near wall region), while the $K-\epsilon$ is used for the free shear flow.

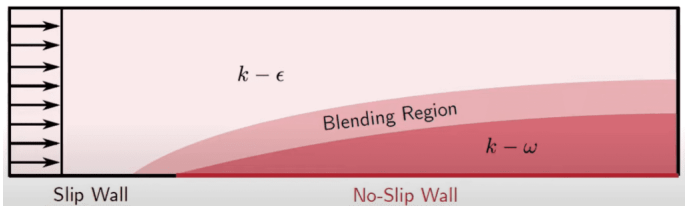

Figure 11: Graphic representation of the SST model [7]

The solver used for this work is Simcenter StarCCM, a multiphysics CFD software, the software also encircles meshing technology. A complete full annulus unsteady simulation on the radial diffuser was carried out.

4.2 Mesh and geometry

The model for the experiment was a 3D vaneless diffuser, with pinched extremity at the inlet. The geometry was modified during the work to analyze the behaviour with respect to stall. In particular, there are four cases:

- Parallel wall
- 0.2^o divergence angle
- 0.5^o divergence angle
- 1.0^o divergence angle

The table below condenses the geometric parameters for the first case.

Through StarCCM software, with the automated mesh command, for each study case a new mesh was generated, apart from the starting one that had already been developed.

The baseline mesh had the following set-up: 969800 cells, 2854955 faces, 1025000 verts. It is worth to highlight these parameters will vary following the geometric

Geometric parameters	
Inlet height	0.003407 m
Outlet height	0.002398 m
Inlet radius	0.002754 m
Outlet radius	0.05256 m

Table 1: Most important geometrical values

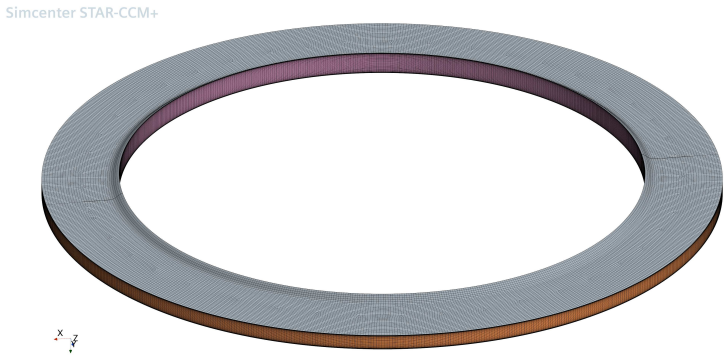

Figure 12: Rendering of the final mesh

configurations. The mesh sensitivity was already verified as part of another work. Hereby are reported the successive enhancement did to the mesh to increase the sensitivity with respect to the inlet flow angle, N is the number of cells.

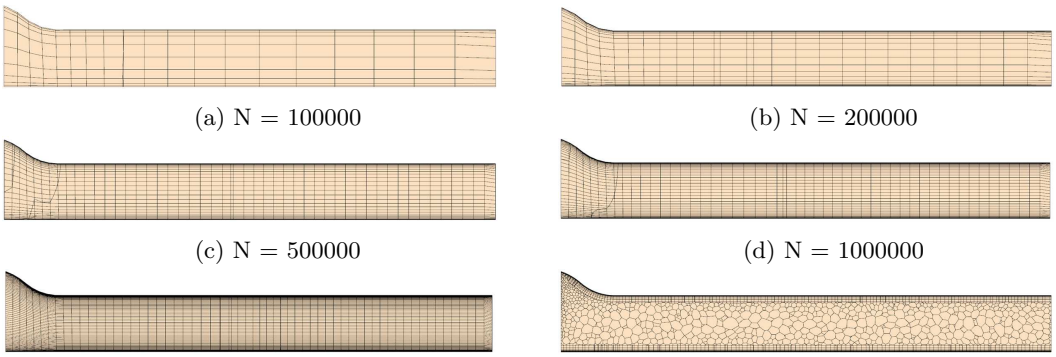

(a) N = 100000

(b) N = 200000

(c) N = 500000

(d) N = 1000000

(e) N = 1600000

(f) N = 4000000

Figure 13: Different mesh with increasing number of cells

The graph below shows the inlet flow angle against number of cells divided by 10^6.

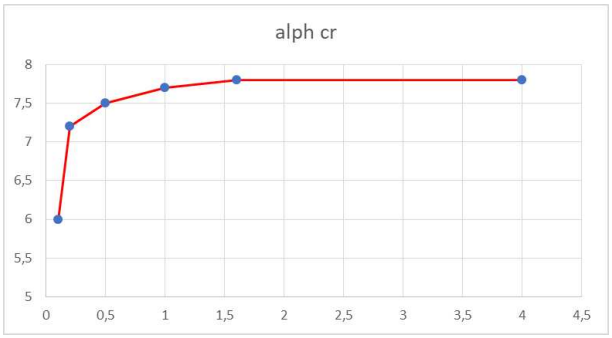

Figure 14: Graph α - $N/10^6$

The diffuser is the only part that belongs to the body group in the 3D CAD, while the design parameters are the radial length and the upper wall angle. As briefly discussed in the previous chapter, those quantities are related by the $r-\theta$ equation

4.3 Parallel wall case

The standard case, took as a reference, is the first analyzed. In this frame, the inlet flow condition is given by modifying the physics values, in the inlet region of the diffuser, that is referred to as "mixing plane diffuser". Therefore the first angle that has been imposed is 20^o, afterwards the angle was constantly reduced until the stall occured, generally the simulations were stopped around 7^o, because the stall already occured. Meanwhile, the c_p and the η were kept track of.
Tipically, every simulations required 4 hours distributed on 72 processors. This time was sufficient to reproduce a physical span time of 0.02 seconds. It was crucial to simulate at least 50 rotations of the impeller, even though the compressor was not part of the simulations, because the stability of the flow field had to be ensured.

To observe the flow field two views were employed, while y was the shaft axis, one on the $x-z$ plane (so called R_θ) and on the $x-y$ plane (R_x). The first one is commonly used to detect stall cells, while the second one is useful to describe the boundary layer separation and the blockage in the channel. The section displayed in all the figures is a cut of the diffuser at 0.2067 m of height. At the meantime, the R_x views are cut in the vertical plane but with evaluated as different angles, for simplicity the images will display the same cut, if it is not stated otherwise.

The main parameters to visualize the flow field behaviour are the absolute total

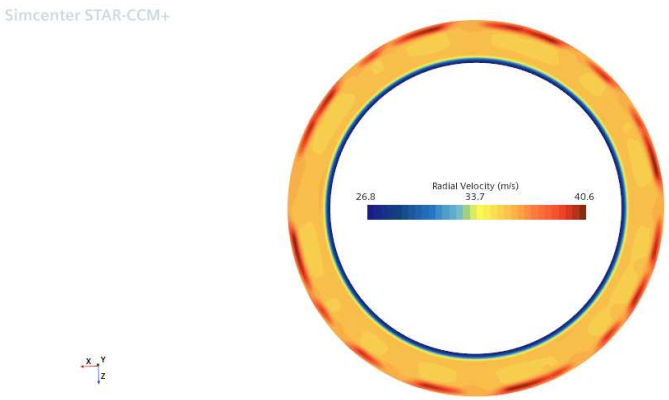

Figure 15: Visualization of a non critical flow field at 20^o

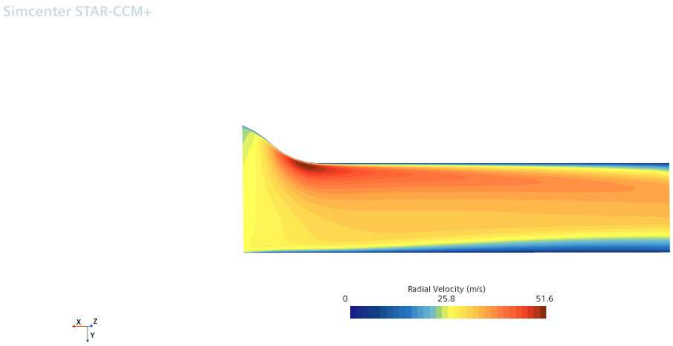

Figure 16: Visualization of a non critical flow field at 20^o

pressure and the radial velocity, however different criteria can be displayed, as axial velocity, static pressure or flow density.
In the "plots" section different features are presented, as the mass flow with respect to physical time, the angle and the number of iterations, the c_p, η or the residuals.

The flow fields displayed as a function of the radial velocity are shown above. It can be seen that in the outlet region of the diffuser the flow starts to re-circulate, therefore backflow regions are formed. At 12^o the flow field is still stable, even though the snapshot shows low speed areas near the exit of the diffuser. Until 10^o the pattern tends to be symmetrical, while at 9^o the structure of the flow field is skewered, the loss of the symmetry is a critical criterion for asserting the stall occurrence. However, beyond the stall initiation phenomenon, the reduction of the radial velocity is clear in the images, it is worth to highlight that low speed areas are now diffusing up to the inlet region.

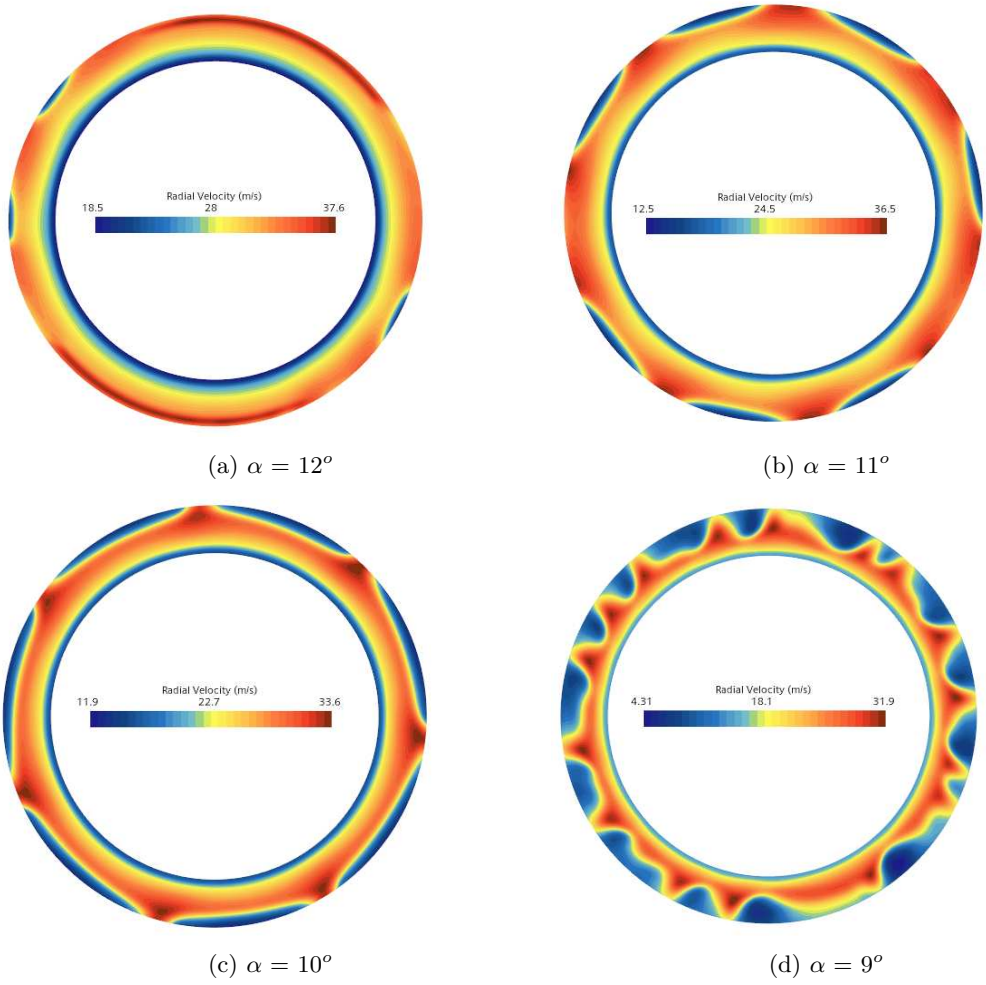

(a) $\alpha = 12^o$ (b) $\alpha = 11^o$

(c) $\alpha = 10^o$ (d) $\alpha = 9^o$

Figure 17: Flow field evolution with respect to the inlet flow angle, annulus view

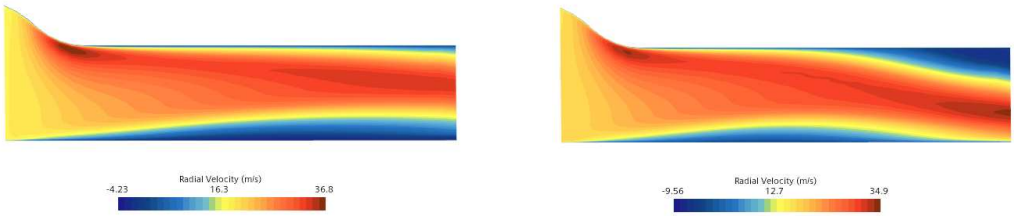

(a) $\alpha = 12^o$ (b) $\alpha = 11^o$

(c) $\alpha = 10^o$ (d) $\alpha = 9^o$

Figure 18: Flow field evolution with respect to the inlet flow angle, channel view

It can be observed that the radial velocity is gradually reducing, in particular, at 9^o it is approaching zero. When this occurs, backflow region starts to appear. In this particular cut the region are not shown, moving closer to hub or shroud the snapshot will display some negative radial velocity zones.
To observe in a different fashion the flow evolution, the R_x view can be employed, this view can show the effects of the hub and shroud presence, as well as the differences at the intlet and at the outlet.
Hence, below are presented the images.

First of all, the boundary layer is thicker with respect to the one shown in figure 5, the velocity is slightly increased at the shroud inlet, due to to the upper pinch. The radial velocity is already negative, this only means that the boundary layer is going to grow due to the friction on the hub side. Next, at 11^o the separation occurs at the shroud in the outlet region, with a similar phenomenon (even though is less intense) at the hub.
At 10^o the flow structure seems to be the same, although there is a difference: the high speed area at the pinch is reduced, as at the outlet. Reducing the inlet flow angle had influenced the flow behavior in the inlet region.
When the stall already occurred, at d, the flow separation at the shroud reached the inlet region, therefore increasing the velocity due to cross section area reduction.
Even if it is not shown in the previous pictures, the evolution of the flow field entails the thickening of boundary layer, afterward the merge of the two layers

on both sides, that will result in a complete blockage and finally the surge.
As mentioned in the paper published by Fujisawa, the flow field appears to be unstable while undergoing stall. Hence, it can be seen the pulsed behaviour. The flow starts to pulse in different section of the diffuser, this can only be shown displaying different section together at the same physical time, as in the next figure.

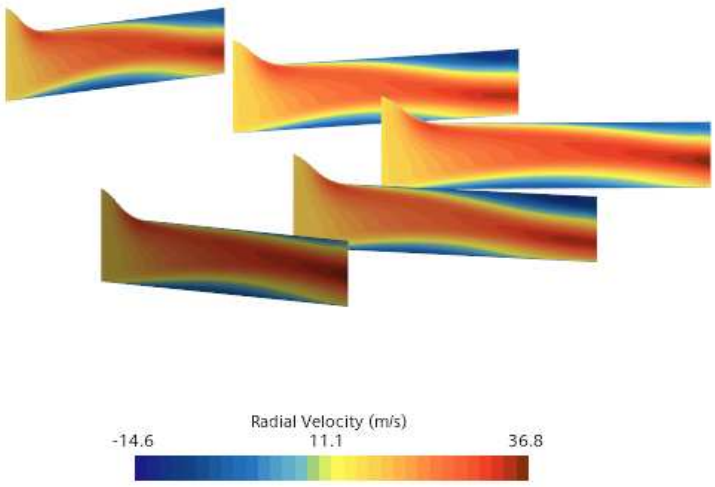

Figure 19: Multiple section of the diffuser in stall condition

It is clear that the flow behaves exactly as depicted before, in the first section there is basically no separation at the shroud, while in the next one the boundary layer increased the thickness. In the middle section the separation region has decreased, while at the hub the changing are almost negligible. Again, moving onto the next section the boundary layer has propagated to the inlet, even though in the last section is slightly reduced.
To find the critical angle at which, according to the literature, the stall cells are formed, it is needed to assess the diffuser's radial velocity distribution with smaller resolution. Hence the angles were reduced gradually from 10° to 9° (that is the possible stall interval according to the flow field) with 0.1° step.
Until this part, the evidence of the stall were only based on the behaviour of the flow in the diffuser, referring to the evolution of the pattern, as aforementioned

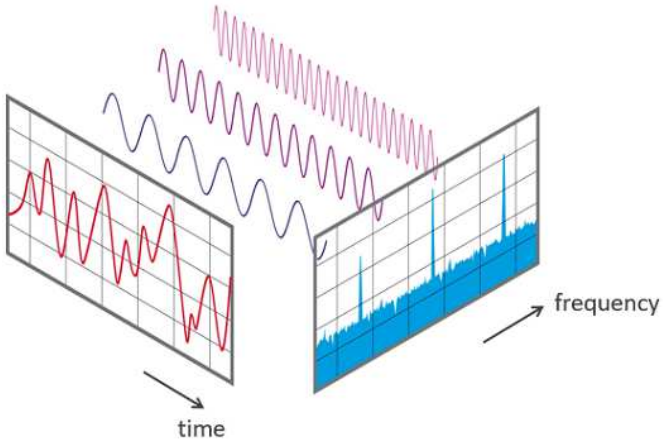

Figure 20: FFT scheme in the time domain [8]

the lost in the symmetry was a sufficient reason to investigate with particular attention that interval. Although this is not a necessary condition, nonetheless is obviously not an objective criterion to determine the critical angle.
Since the flow field visualization is not a sufficient criterion to establish with accuracy the critical angle, the signal analysis is employed. In particular the Fast Fourier Transform (FFT) analysis has been performed on the radial velocity distribution. Specifically, the values were exported from StarCCM to Matlab, then a code to display the 3D graph was developed, exploiting the import function that is a Matlab feature.
Moreover, the fast Fourier transform (FFT) used in this context is the spatial one. Widely used in signal processing, image analysis, and other engineering applications, the FFT facilitates rapid frequency analysis and manipulation of data, making it a fundamental algorithm in digital signal processing. The Fourier analysis converts a signal in its domain (i.e. time for time dependent signals, space for space dependent signals, as in this case) to the frequency domain. This analysis can be carried out using DFT, the main issues regarding this process is the high computational cost, that scales with n^2, where n is the amount of data. FFT exploits factorization to decrease the computational cost, therefore lowering the proportion to $n \log n$.

The spatial FFT is a specific extension of the most general case, it is often use to tackle two-dimensional signals, with the purpose to reveal the frequency content of a the spatial dataset.
The two variables considered hereby are the radial velocity (expressed in m/s) and the angle (degrees), determined on an arbitrary radius, sufficiently distant from both inlet and outlet. The actual FFT data employed were the radial velocity variance, to obtain this value was sufficient to subtract the mean value

to the radial velocity distribution. While the angles pin the velocities on the annulus' radius.
The use of this modified V_θ, is not casual, in fact the parameter is able to show the general fluctuation from the mean value, therefore the peak will occur at the point in which there is the maximum deviation from the mean.
The graph is really helpful to assess the situation in the diffuser, on the x-axis the frequencies are shown, while the y-axis reports the amplitude. The z-axis represents the angles, with a 0.1° precision.

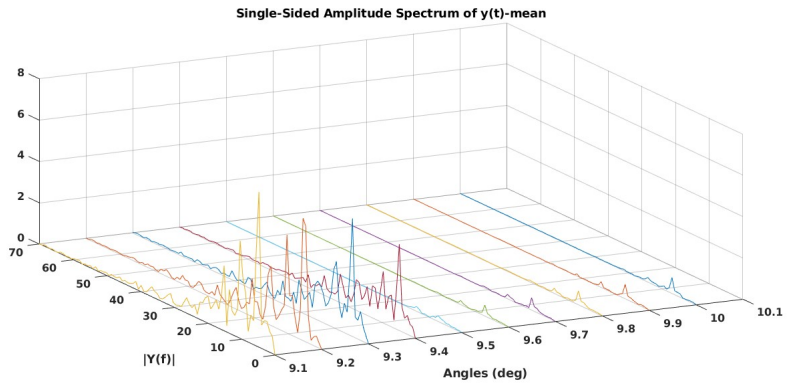

Figure 21: FFT for the parallel wall case

Looking at the graph, the first peak that occurs is the one at 9.4°, with an amplitude around 2.5, a sudden increase with respect to the previous ones. After this condition was achieved, the peaks kept escalating, at 9.1° the amplitude was 4.1. This latter observation is an important feature that has to be taken into account. Therefore there is no evidence of regression in terms of amplitude for the subsequent angles.
Another important remark can be made, in fact it is relevant to underline the smoothness of the signal at, almost, all angles. Obviously, the disturbances and the noise arising at the lower angles are due to the beginning of the stall. As discussed in the previous chapter, the mild stall (i.e. the stall cell formation process) can provoke a slight increase in the noise and vibrations of the component.
Moving forward, with a fixed angle, the maxima are spatially related to each other, therefore the frequencies at which every peak is occurring is proportional to the fundamental mode of the signal. In particular, at 9.4° the frequency is 7.2 and this can be indicated as the natural frequency of the system.
The natural frequency (sometimes can be referred to as eigenfrequency) is the specific frequency component present in the discretized signal that corresponds to a peak in the amplitude spectrum, it indicates a dominant periodic behavior inherent to the original signal.

The frequency that has been found has a profound meaning. Since the analysis is spatial, the formula for the Fourier formalism is:

$$F(k) = \int_{-\infty}^{\infty} f(x)\, e^{-i2\pi kx}\, dx$$

For the diffuser case, the space is not linear, thus the spatial domain is swept by the actual θ variable and the signal is observed only around a single circumference, hence:

$$F(k) = \int_{0}^{2\pi} f(\theta)\, e^{-i2\pi k\theta}\, d\theta$$

However, there is an important feature that is revealed by the space-frequency transform, namely the meaning of the natural frequency. This value is linked with the space fluctuations of the radial velocity, the peak shows the way of these deviations, therefore suggesting that the frequency, approximated to the closest integer, represents the number of stall cells.
This statement is in perfect agreement with the flow field that is displayed at 10°, which is shown in the following image:

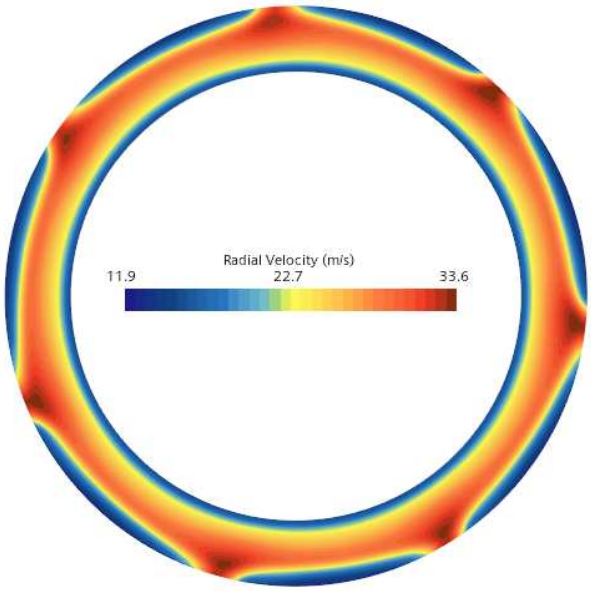

Figure 22: Flow field behaviour

Although the critical angle assessed is at 9.4°, here it can be seen there are 7

distinct regions, in which the radial velocity shows some values with high variance.
This result confirms the Senoo and Kinoshita theory, but as already mentioned, this analysis might show different results for the next cases, due to the geometry variation.
Whether or not the stall mechanism (i.e. stall cells formation) described by Senoo et Al. is accurate enough to describe the phenomenon within divergent wall diffusers, is the real challenge of the work. This explains why the analysis had to be completely unfolded in detail.
Before investigating new geometries, there is one last comment that has to be made. As part of another work, that it can not be mentioned here due to confidentiality reasons, the critical angle was established at 8.7°. The simulation, in that experiment, considered the set-up for the whole machine, therefore with the compressor, the diffuser and the volute. This difference found in the angles, is caused by the set-up, but may suggest that stall is driven by the diffuser, as it reaches the critical angle before the whole system.

4.4 Divergent wall case: 0.2°

As discussed at the beginning of the chapter, the variation in the upper wall angle modifies the geometry of the outlet area, moreover it is necessary to compensate the increase of frontal area with a reduction of the outlet radius, doing so enables the comparison between different cases, since they show same grade of diffusion.

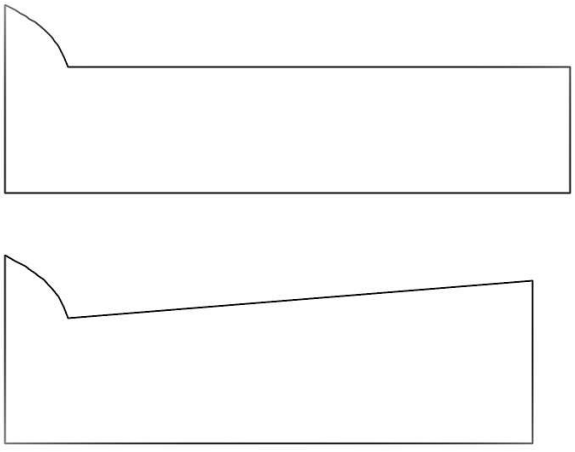

Figure 23: Geometry variation from parallel to divergent

In the sketch here shown, the proportion are neither real nor to scale. It is important to visualize the reduction in the outlet radius and the increase in the outlet height, compensating the outlet areas variation.

The r_θ view is shown below, for every inlet flow angle.

These six views have both similarities and differences from the parallel wall case. First of all, the radial pattern with high symmetricality is completely lost. Moreover, the radial velocities are higher than before, at 12° for example, the peak is at 38.2 m/s, while in the previous case was 37.6 m/s. In addition, the radial velocity becomes negative at 11° already, with small backflow regions formed at the outlet.
Those areas increased in terms of volume and numbers (fig 14.c), which then propagated toward the inlet, as shown at 9°.
At the next corner, the elongated arch-like structure can be seen, while the pre-existing bubbles remained present, some of them detaching themselves from the outlet.
In the last snapshot the previous situation has evolved leading to the presence of structures reminiscent of stall cells.
In a first instance, stall seems to occur between 9° and 8°, although this hypothesis is reasonable, before starting the Fourier analysis it is appropriate to look at the flow in the channel and how the boundary layer is behaving, since it may be different from before.

The images above show the behaviour of the flow from the so-called r_x view. Again, since this is a new case, are presented six different graphs. It is worth to assert that the chromatic scale used is the same for all the cases, thus it is glaringly obvious that the speeds involved are different, as already discussed earlier for the past r_θ views.
A comment has to be made to explain the reason behind the radial acceleration outward. The diffuser decreases the speed of the fluid thus recovering the static pressure, this phenomenon should be emphasized since the channel is divergent. The Area-velocity relationship yields:

$$\frac{dA}{A} = (M^2 - 1)\frac{dv}{v}$$

Where M is the Mach number, v is the velocity. Since the flow is subsonic, it is true that:

$$\frac{dA}{A} > 0 \implies \frac{dv}{v} < 0$$

As expected, but due to the boundary layer separation happening at the hub, there is a reduction in the outlet area, inducing therefore an acceleration in the flow. This is why the radial velocity is increasing outward, paradoxically, compared to the intended.
Again, there are few resemblances and some discrepancies. The main similarity is the contrasting hub and shroud boundary layer separation, a phenomenon analyzed earlier and explained by Fujisawa. Although the radial velocity for this

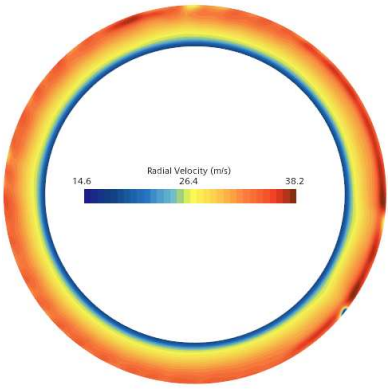

(a) $\alpha = 12^o$

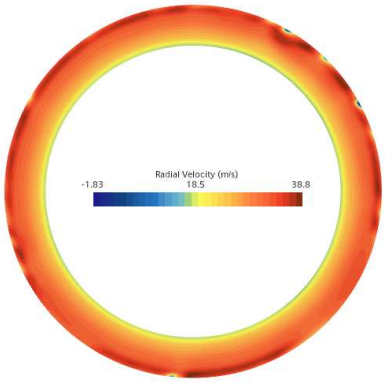

(b) $\alpha = 11^o$

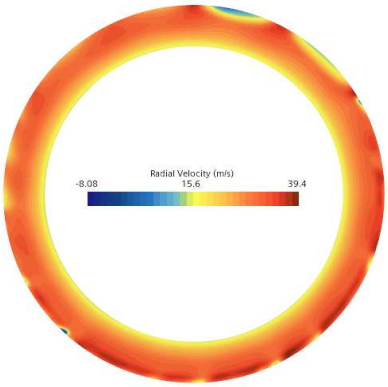

(c) $\alpha = 10^o$

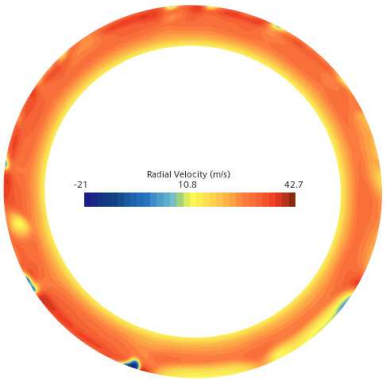

(d) $\alpha = 9^o$

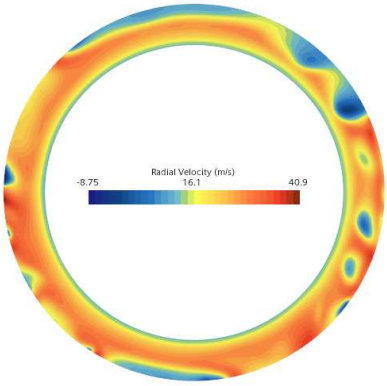

(e) $\alpha = 8^o$

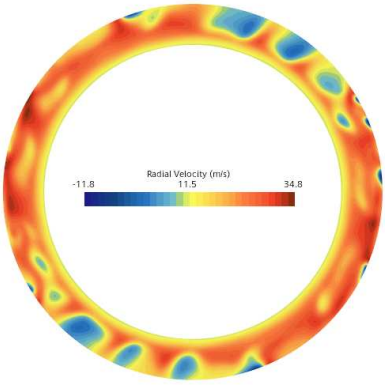

(f) $\alpha = 7^o$

Figure 24: Flow field evolution with respect to the inlet flow angle, annulus view

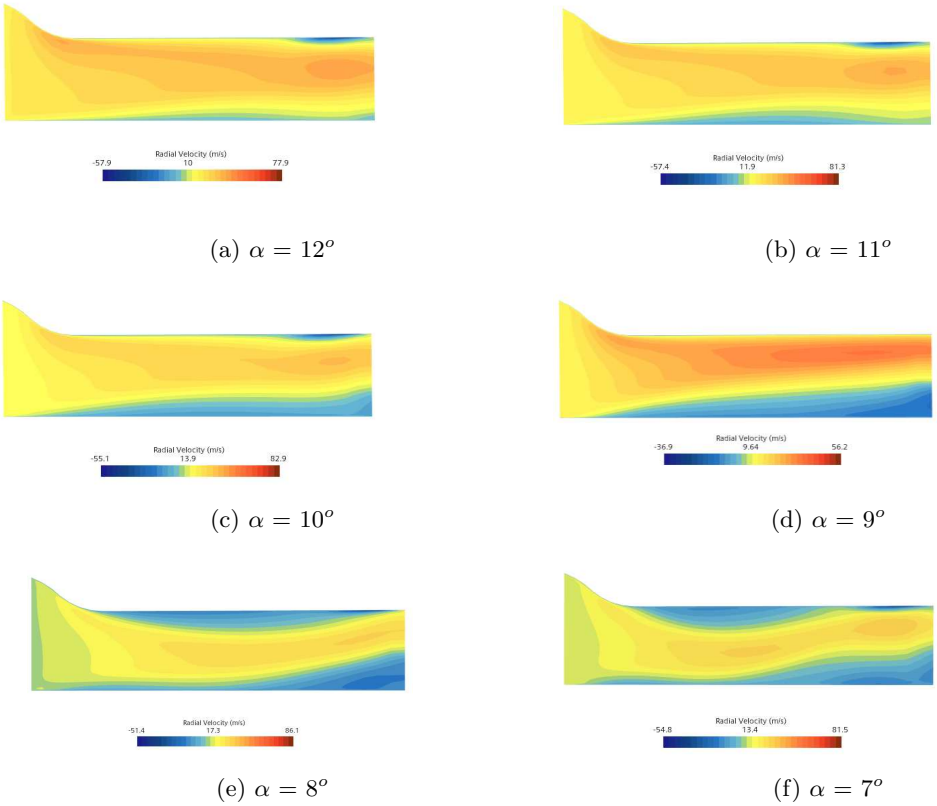

(a) $\alpha = 12^o$ (b) $\alpha = 11^o$

(c) $\alpha = 10^o$ (d) $\alpha = 9^o$

(e) $\alpha = 8^o$ (f) $\alpha = 7^o$

Figure 25: Flow field evolution with respect to the inlet flow angle, channel view

case was lower, generally. Even in this likeness an odd fact can be found: the divergent diffuser here considered, delays the mechanism of the double boundary layer separation. As a matter of fact this pattern starts at 11° for the study case, while for this configuration, the flow appears to be pulsed starting from 8°.

As opposed to the other result, there is not a transition in the boundary layer separation process. With parallel wall the propagation was gradual, while here the simultaneous detachments occurred almost in the mid-span at shroud. Before this previously seen behaviour, the boundary layer growth at the hub is remarkable. At 9° (fig 15.d) the maximum thickness is reached due to the pressure gradient increasing downward, then the outlet area is minimized, in that context thus the radial velocity is maximized.

The overall stall pattern seems to have some similar feature to the parallel wall one, but at the same time there is a difference in the evolution of the process. This may suggest new explanation has to be found or the stall cell mechanism has to be extended for different geometries.

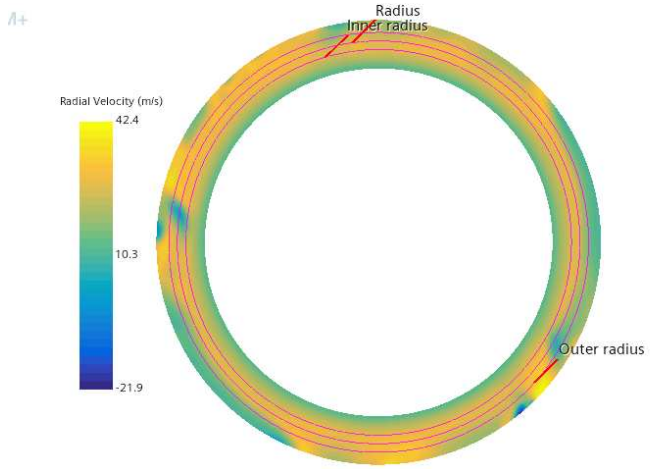

Figure 26: Geometry variation from parallel to divergent

The spatial FFT enables to find the modes of the signal, but for the next cases the analysis may be biased, since stall cells could not sufficiently describe the real mechanism. In order to ensure the results do not depend on the radius position, for this instance the distribution of radial velocities were computed around three radii, as shown in the above picture. The colours were modified for the only purpose of showing the circumferences.
In fact, the radial velocity that is shown in every r_θ view, is evaluated at a specific cut and will surely be different if the cut is moved closer to hub or shroud. Moreover, the same can be said for the distribution along the radius, just looking from channel prospective it is trivia to understand the changes in the average value (and its deviation) from inlet to outlet.
Using three different position was crucial to determine whether or not the method was coherent and not to validate theory behind stall mechanism, this had to be highlighted.
The Spatial FFT for the middle radius is shown here, followed by the other two radii distribution.

In the graph the first peak can be observed to appear at 8.7°, doubling the previous maximum's value. Although this is not the first amplitude peak. The trend is different from what expected, the decrease in amplitude is obvious until 8.3°, then again the maxima are showing coherent behaviour. In particular it can be stated the frequency difference existing between all the maxima and the peak at 8.2°. Another discrepancies is the amount of noise, easily observable in this graph. To summarize, there is not a distinctive transition that allows to state a critical angle and the background noise has higher levels with respect to parallel wall case, nonetheless the amplitude are halved regarding the previous scenario.

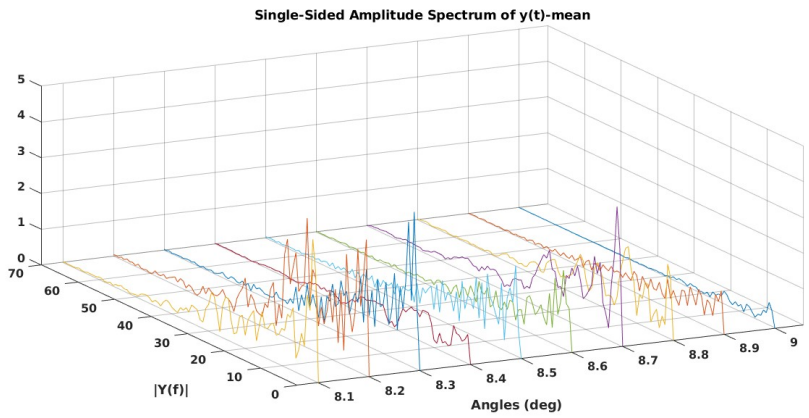

Figure 27: FFT for the 0.2° divergent case

The main reason can be the fact stall cells pattern can not describe properly stall phenomenon for this divergent case, even if the supposed cells can be found and are perfectly distinguished in the images. Therefore the analysis may suggest that there is a hybrid mechanism able to explain the stall. As argued for the channel views, it is possible that a different mechanism took place at first instance and then the cells developed regularly, given that the pulsed behavior occurred belatedly.
This assumption is consistent precisely because of the critical angle, that is lower than the parallel wall one, thus the divergent channel would be effective in delaying stall.
To confirm and discuss the results here are shown the FFT analysis for the two different distribution.

The two results can be compared to the main one, demonstrating how the spectral analysis is not affected by the chosen distribution among the different radii. However there exists few differences, but they do not compromise the key outcome (i.e. the possible critical angle).
Starting from the outer radius one, the trend follows the same up and down shown by the previous graph, in fact the first peak occurs at 8.7° and the second one appears to be again at 8.3°.
Moreover the peaks at 8.4°, that were stretched out before, are now distinct and distant from each other. The peak at 8.2° is shifted toward a smaller frequency with respect to the past one. This is associated with a decrease in general background noise.
The inner radius graph shows almost the opposite features compared with the outer one. The trend already shown subsists, with the same critical angles, but the general pattern differs from the principal one.

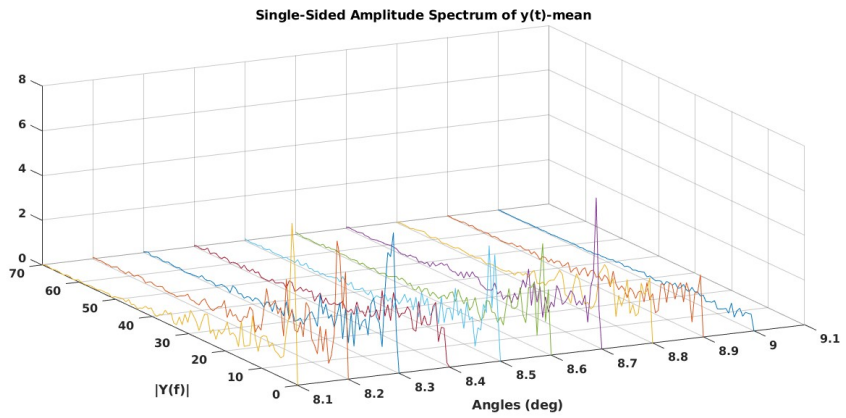

Figure 28: Outer radius FFT for the 0.2° divergent case

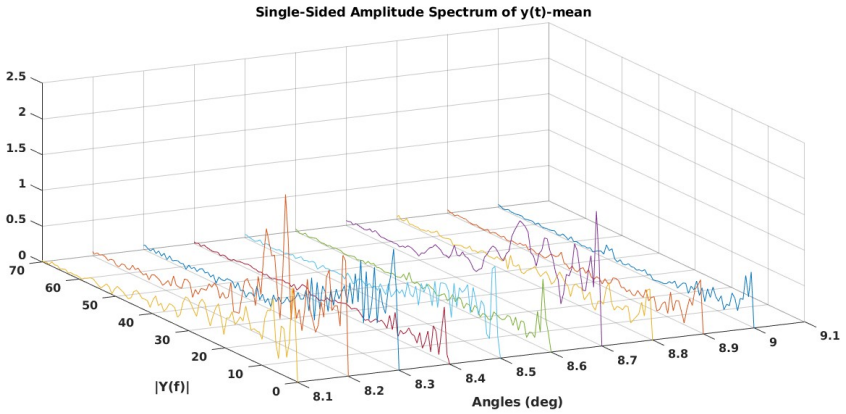

Figure 29: Inner radius FFT for the 0.2° divergent case

In this case the noise is higher than before and than the first graph, in particular it can be observed an increase for the last angles. Even if the peaks show, qualitatively, similar maxima, the amplitude is smaller than the other cases and for a fixed angle, there are closer peaks rather than a distinct one with much smaller maxima. For example, this happens at 8.8° and 8.7°, but as well at 8.3° and 8.2°.
The peak at 8.2° is shifted toward a larger frequency, in contrast with the outer radius, moreover there is a halving of the maximum amplitude at 8.1°.
The two graphs can be used to draw some important conclusions:

- the method is coherent;
- the behaviour of the maxima of the peaks is non sufficient to invalidate the stall cells theory for divergent channels;
- the higher noise demonstrates a bigger radial velocity oscillations, probably due to the radius enclosing part of the mixing zone, that is generally more turbulent;
- the link between frequencies and stall cells number is almost lost;
- the upper wall angle being negligible can be the reason why stall mechanism partially resemble the previous one, although the latter can not be simply explained by stall cells.

4.5 Divergent wall case: $0.5°$

This second divergent case presents an upper wall angle (i.e. the angle for the divergent wall at shroud) of $0.5°$ which reduced the outlet radius, according to the previously discussed formula. Starting from this angle it will be clear if the pattern for stall would be the same or not.
Again, the boundary layer separation had strong influence on the flow inside the diffuser, in fact the induction of an increase in the radial velocity is still effective.
Before moving forward the views are presented.

Beginning with the flow field at $12°$ some small low speed areas can be observed near the outlet region. The radial velocity is increasing outward, as before, suggesting the same behaviour of the boundary layer, although the gradient seems to be less intense. The maximum radial velocity is higher than the previous case, but it is constantly lowering the value as the inlet flow angle diminishes, in contrast with what was stated in parallel wall and first divergent cases, where the trend was in the opposite direction.
At $11°$ the pattern evolution is still not clear, the average velocity at inlet increased, while the gradient of radial velocity is now more severe. The dark red areas indicate regions in which the radial velocity is the highest within the annulus, in particular they are almost evenly-spaced.
The maximum radial velocity, that is 38.3 m/s remains constant for the next scenario, the general conditions in the diffuser also do not seem to have changed. The average velocity is decreased,
At $9°$ something have changed, if until now there was no hint of a possible stall, for this angle what immediately strikes is the presence of these bubbles, but they are different from classic stall cells that have been recognized. In fact, stall cells develop from backflow regions or vortexes regions. While from the snapshot it is clear that these regions are high speed areas.
Again, can be only assumed a partial development similar to the stall cells one, to have a better understanding of the different phenomena channel views are

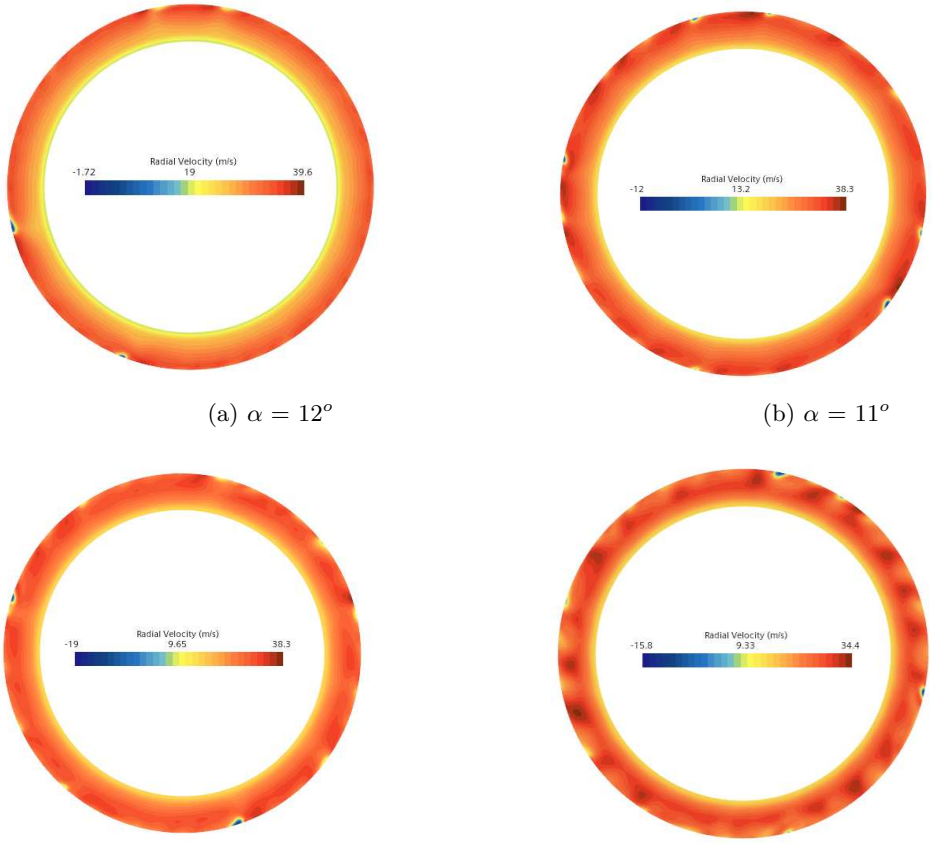

(a) $\alpha = 12^o$ (b) $\alpha = 11^o$

(c) $\alpha = 10^o$ (d) $\alpha = 9^o$

Figure 30: Flow field evolution with respect to the inlet flow angle, annulus view

shown as well.

The stall is already developed at 9°, so it was not necessary to display other images.
The boundary layer separation, as expected, influenced noticeably the flow field evolution through the different stages of the stall.
There is a thickening of the layer at the hub, meanwhile the shroud seems to be not affected by this behaviour. In particular, it is worth to point out that in fact there is a low speed region at the shroud, but it is bearably observable.
In this context, the boundary layer at 9° completely decrease the outlet area, making it half of the starting one, the flow radial velocity is increased as a consequence.
A key factor that has to be taken into account, is the dimension of the channel.

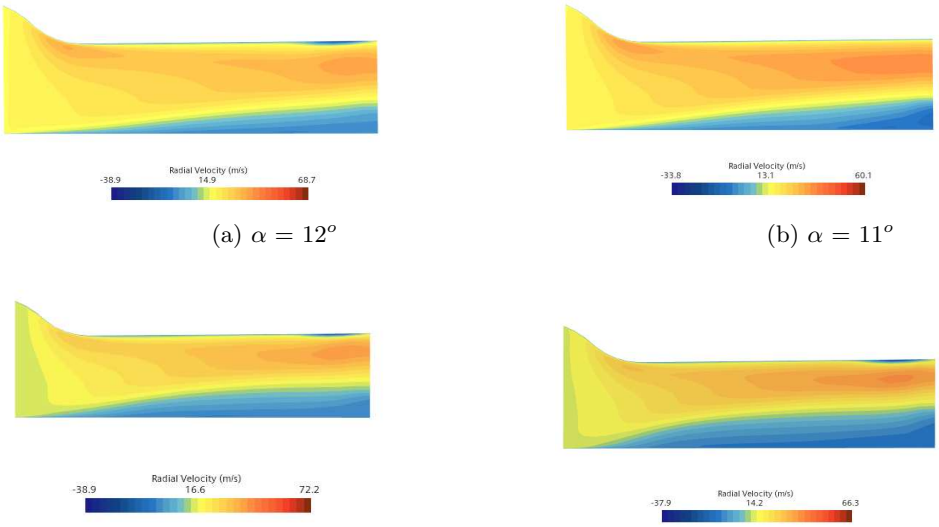

(a) $\alpha = 12^o$ (b) $\alpha = 11^o$

(c) $\alpha = 10^o$ (d) $\alpha = 9^o$

Figure 31: Flow field evolution with respect to the inlet flow angle, channel view

Since the outlet radius is reduced then there is a shortened path for the flow, increasing the pressure and the pressure gradient is increasing the thickness of the boundary layer, due to the fact that the upper wall is divergent the flow will follow in a more regular manner the surface. It is easy to understand this simply looking at the experimental results of airflow being inflected onto the flat foil.
Even if the results just presented show the theory of stall cells is not accurate anymore, the spatial FFT can demonstrate what are the existing features in this case. Since the coherence of the method was previously discussed, here only one graph is reported.

This interval was the one with highest probability of stall development, even the flow field from r_θ view is points this way, but from this graph it can be stated that the spatial FFT does not show any sudden increase in the signal peaks. It is due to the loss of accuracy of stall cells theory.
It is still possible to find a critical angle, that is 8.9°, since the first sudden increase happens for this angle. At 9.1° the peak has a proper frequency value of 21.3. This is a high number for stall cells, but the flow field at 9° shows exactly 21 different region within the annulus, as is presented in the magnification of image 20d here reported.

Mainly, noise drastically increased. It can be observed that around every maximum there is not a smooth transition. It is difficult to find a single distinct

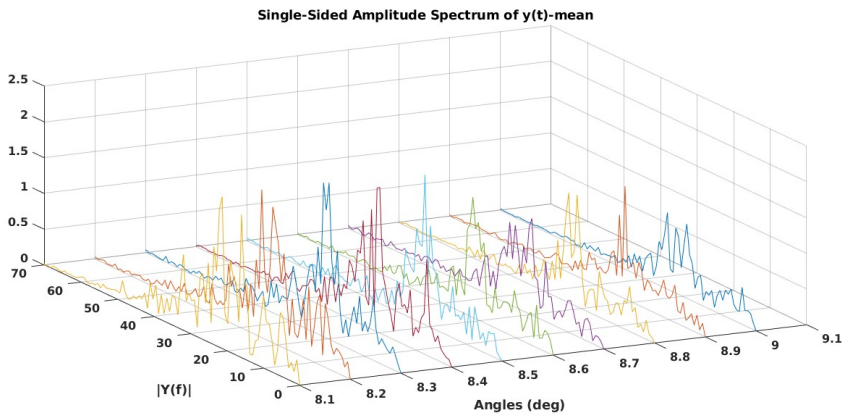

Figure 32: FFT for the 0.5° divergent case

peak for a fixed angle, all the maxima are close to each other. This can explain why the amplitude is halved with respect to the parallel wall case. In fact the most distinguished peak reaches an amplitude of 1.5, at 8.3°.
For this range, however some few considerations can still be made. At 9° the maxima are close to each other, they have different frequencies, the average of those frequencies is then found for the next angle, at 8.9° peak.
This mechanism is quite similar to the cells merging process happening in parallel wall case. However, the general analysis, especially the noise, shows how it is not possible to base the stall evolution on stall cells. For this case the pattern is totally different from before, suggesting the previous case was comparable with the first one because of the divergent angle that was still small and approaching zero, thus parallel wall.
So far, the two cases with divergent wall have unearthed the limits of the classical theory, highlighting the requirement for a modification or a completely new description for stall mechanism. The last case will provide the ultimate answer.

4.6 Divergent wall case: 1°

The last case here introduced is a divergent wall case, with a divergent angle of 1°.

The snapshot for the r_θ view are show above.
The results that are going to be exposed will make it understandable why a further increase in the angle would have been unnecessary. In fact, the dimension of the channel is getting shorter, thus complicating the diffusion factor that also relies on the length of the channel.
As it can be seen from the images, the flow field is similar to the case with 0.5°, rather than the 0.2° or the main study case. The maximum radial velocities are

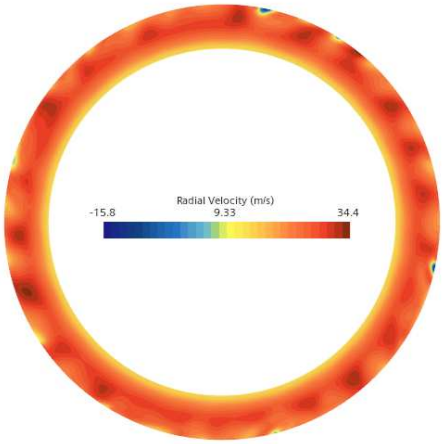

Figure 33: Magnification of image 30d

still higher than every other case before.
About the flow structures some hint highlight the velocity gradient, that is progressively getting harsh from 12° to 9°, but its transition (or regression) is more linear than before.
The behaviour suggest that when the upper wall angle is not negligible (therefore 0.2° can be approximated to zero rather than a big angle), the solution to stall mechanism can not rely on stall cells, as the last two cases has nothing in common with stall cells explanation but the speed regions.
Looking at the fluid behaviour from r_x view other remarks can be made.

The flow field evolution displayed gives some hint. First of all the boundary layer behaviour, the same problem appeared in the previous case and, even if with some discrepancies, in the 0.2° case.
The radial velocity is greater in average, probably due to the fact the boundary layer separates more robustly and thus induces a higher reduction for the cross section.
In this context the separation happens almost exclusively to the hub. Due to the divergence angle, now also the junction between pinch and wall causes some velocity fluctuations.
Eventually the stall occurred and the vertical profile of the layer reaches a maximum and then decrease, realizing a convergent-divergent channel. As a consequence, the flow is effectively slowed down and subsequently the average radial velocity decreased.
This explains the different speed areas in the r_θ view, figure 32d. It is worth to highlight that the channel views strictly depend on the position of the section, so the behaviour is similar in some cuts, while different in others. This is why there is not a low speed circular arc at the outlet, but only few regions.
Even if the previous analysis leads the way to a new theory, it remains valuable

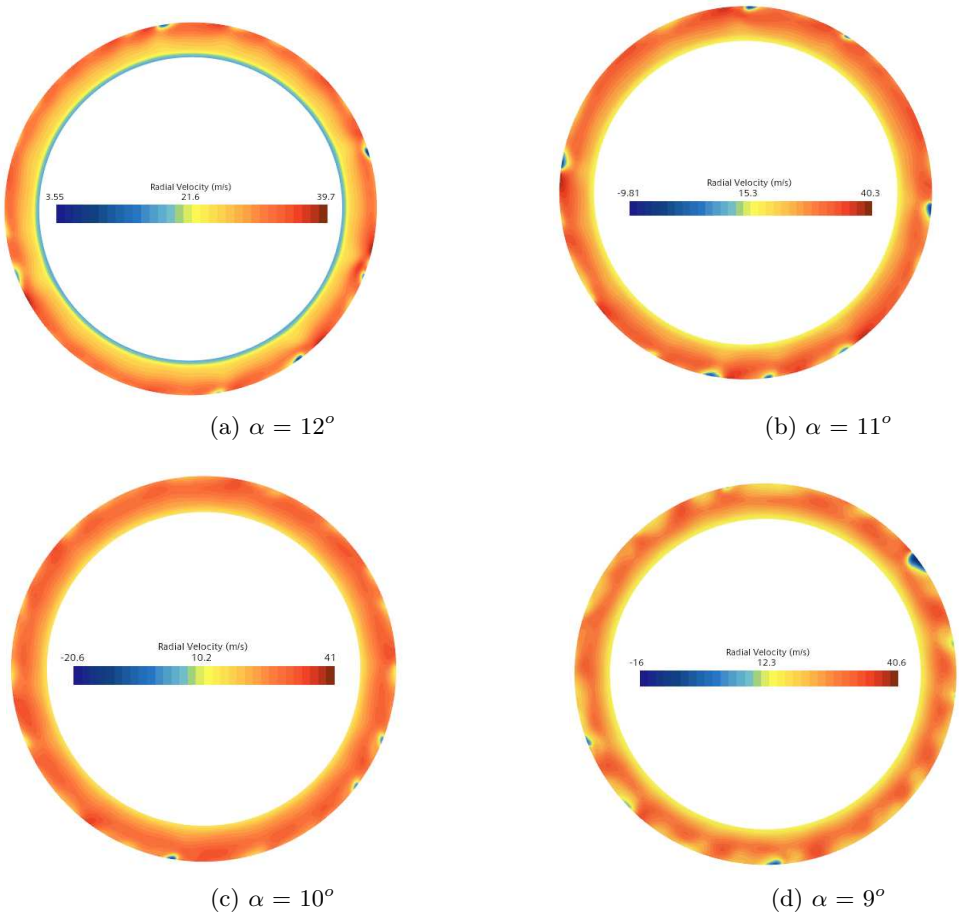

(a) $\alpha = 12^o$ (b) $\alpha = 11^o$

(c) $\alpha = 10^o$ (d) $\alpha = 9^o$

Figure 34: Flow field evolution with respect to the inlet flow angle, annulus view

to look at spatial FFT that may give new hints.
The most interesting feature is stall development in a different interval. As can be seen from the graph, the classical range for the critical angle is shifted of 1°, with respect to the other divergent scenarios. In fact the critical angle is 8.7°, since the first amplitude peak appears at this value. Therefore, this particular degree of divergence actually anticipates the stall, as opposed to what would be necessary.

Regarding the amplitude, even in this case the average amplitude decreased, with the most intense peak around 1.3 occurring at 9.2°.
Again there is a noise problem, suggesting the various phenomena happening within the diffuser, this is due to different fluctuations of the radial velocity.

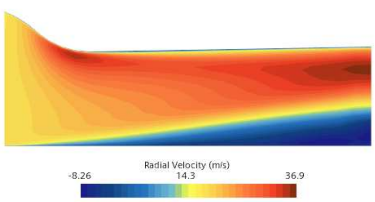

(a) $\alpha = 12^o$

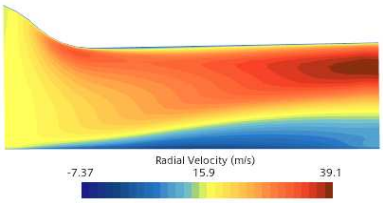

(b) $\alpha = 11^o$

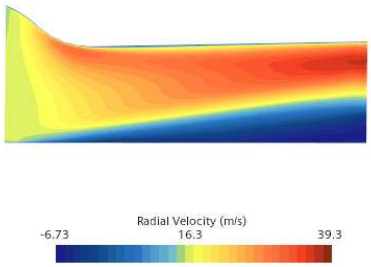

(c) $\alpha = 10^o$

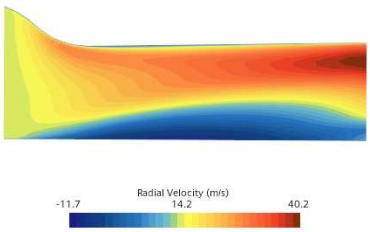

(d) $\alpha = 9^o$

Figure 35: Flow field evolution with respect to the inlet flow angle, channel view

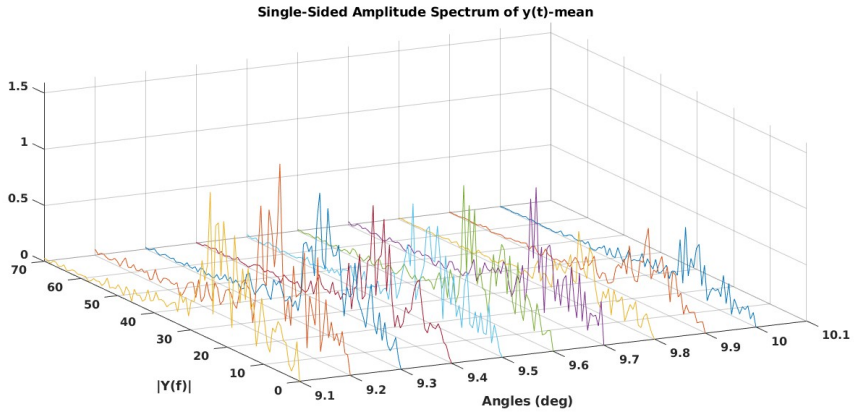

Figure 36: FFT for the 1° divergent case

This last model presented confirms the need of an extended theory for divergent wall, since stall cells, as discussed many time, can not manages to capture the nuances of fluid dynamic behavior in this conditions.
However, even though delay stall is the main objective for this components, it

is also fundamental to assess the performance and their variations while the diffuser is undergoing stall condition, to better understand the response to a non-design operational mode, also to find a way for the trade-off.

5 Results

In the introduction was mentioned the performance tracking, since the diffuser must provide high-level performance, regardless of how the stall evolves or the geometry varies.
The geometry impact is less important in this context, unlike the case of a volute, for instance. However, for larger centrifugal compressor, it can influence the decision, this is why it has to be taken into account.
The most important factors, are the three parameters mentioned in chapter 2. In fact, the losses across the diffuser may compromise the whole machines, especially for centrifugal compressor working with high variable mass flow (e.g. APU compressors).
The loss performance coefficient is hereby recalled:

$$\eta = \frac{P_t^{in} - P_t^{out}}{P_t^{in} - P_s^{in}}$$

For the pressure coefficient or pressure recovery, this is an other side of the same parameter. The former one emphasizes losses and acts as a efficiency factor, thus it has a striker impact.

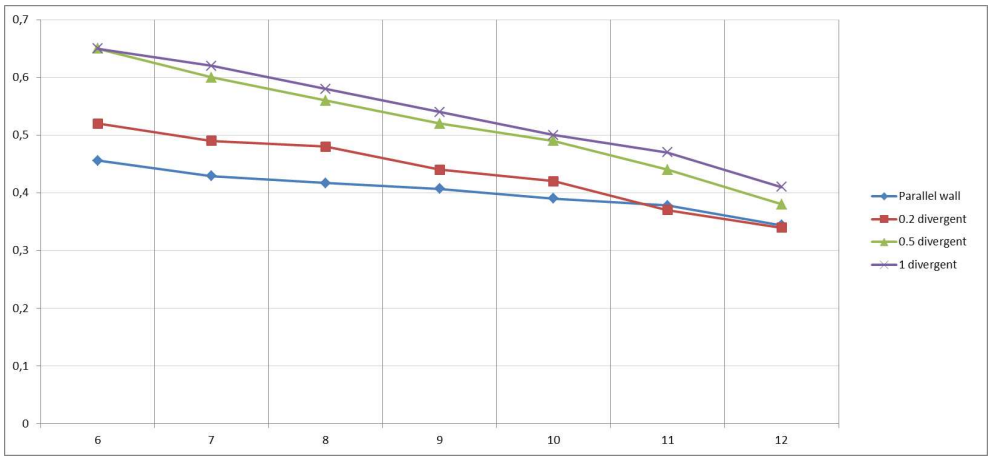

Figure 37: Losses vs Inlet Flow Angles

The graph here represent the variation of the losses against the inlet flow angle. First of all, the parallel wall diffuser is the one showing the best regression, so the minor losses happen in the first case.
On top of that, there is a correlation between the divergent angle and losses. As the graph presents, the first divergent scenario, 0.2°, has the best regression among the divergent diffuser. The losses worsen with the increase of the divergence angle. Therefore, the last case, 0.1° is the worst scenario, with the lowest

loss coefficient that can not match the highest loss coefficient for the parallel wall case.
Since stall is a phenomenon that compromises the mass flow, is important to characterize the diffuser performance through flux capacity under critical condition (the same is done for choking limits).
The graph below shows the different path for all four cases. As expected the parallel wall case provide the highest mass flow rate, while again this parameter get worse if the upper wall angle increases.
The peculiarity in this graph is the general trend, in this context it can be observed how the divergent scenarios show an almost linear behaviour, while the parallel wall case has a more discontinuous decrease.

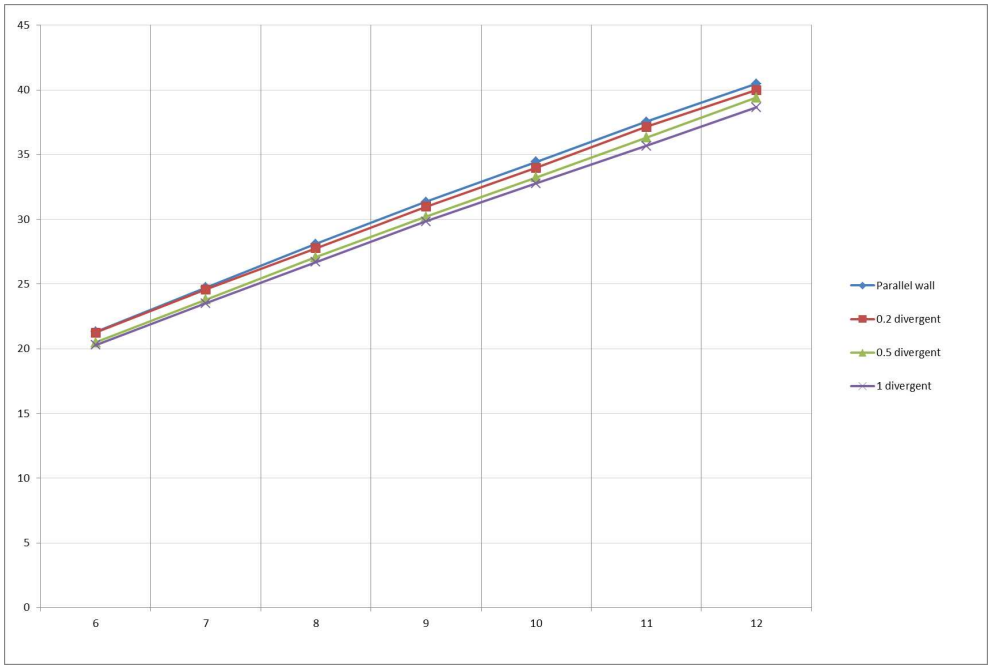

Figure 38: Mass flow (g/s) vs Inlet Flow Angles

Also for this graph, only the 0.2° divergent case shown the best trend, almost matching the parallel wall diffuser. This is why it would be the best choice since the stall is delayed, while mass flow and losses are quite similar to parallel wall case.
On top on these reasons, the 0.2° presents similar stall mechanism, although not identical, to the main study case.

6 Future work and conclusions

The following are details on which future work should focus and conclusions that summarize and review the work done

6.1 Future Work

A number of questions emerged from this work that future studies will need to answer. In particular:

- Geometry influence on stall mechanism
- Stall cells limits theory in divergent diffuser
- Spatial FFT limits in analyzing flow in divergent diffuser
- Feasibility of hybrid parallel-divergent diffuser
- Laboratory experiment to validate simulations

6.2 Conclusion

In the presented work, a complete fluid dynamic analysis of a diffuser with various geometries is performed.
The CFD employed the unsteady RANS coupled with the SST $k-\omega$ turbulence model. The solver in which the analysis and the models were implemented was StarCCM. Post-processing and data sorting were done with Matlab, through a code able to develop Fourier Analysis in spatial domain.
The main objective of the work was to assess critical angles and relate them to geometrical changes. This was done successfully and the results shows the $0.2°$ and $0.5°$ cases delayed stall with respect to parallel wall diffuser, while $1°$ divergent diffuser anticipated the stall, even though the difference for the inlet flow angle was about $0.4°$.
Most of the work was based on stall theory, since it is yet a complicate subject. While the analysis focused also on practical results, such as the influence of the geometry on losses and mass flow rate.
The increase in the upper wall angle, or divergence angle, is related to a general decrease in the performance, this was unveiled by the data. Moreover, the decrease in the mass flow behaves more linearly in divergent diffuser, due to their one-side boundary layer separation.
Nevertheless, the investigation on stall mechanism decreed that stall cells theory is no longer applicable when the angle of divergence is not negligible, as shown for the last two scenarios.
As mentioned earlier, the possibility of hybrid solution can be an interesting path to take into consideration for future studies.
This research lays the foundation for new analysis and experiments, as indicated in the previous section, especially for the stall investigation, in order to obtain more stable and efficient diffusers.

References

[1] VAN DEN BRAEMBUSSCHE, Rene. Design and Analysis of Centrifugal Compressors. John Wiley & Sons, 14 Jan. 2019

[2] Zheng, X., Huang, Q., and Liu, A. (May 3, 2016). "Loss Mechanisms and Flow Control for Improved Efficiency of a Centrifugal Compressor at High Inlet Prewhirl." ASME. J. Turbomach. October 2016; 138(10): 101011. https://doi.org/10.1115/1.4033216

[3] Omidi, Mohammad, Shu-Jie Liu, Soheil Mohtaram, Hui-Tian Lu, and Hong-Chao Zhang. 2019. "Improving Centrifugal Compressor Performance by Optimizing the Design of Impellers Using Genetic Algorithm and Computational Fluid Dynamics Methods" Sustainability 11, no. 19: 5409. https://doi.org/10.3390/su11195409

[4] V. V. N. K. Satish Koyyalamudi, Quamber H. Nagpurwala, "Stall Margin Improvement in a Centrifugal Compressor through Inducer Casing Treatment", International Journal of Rotating Machinery, vol. 2016, Article ID 2371524, 19 pages, 2016. https://doi.org/10.1155/2016/2371524

[5] Anderson, John D. (2007). Fundamentals of Aerodynamics (4th ed.). McGraw-Hill

[6] Franck, Nicoud. (2007). Unsteady flows modeling and computation

[7] "[CFD] The k-omega Turbulence Model." Fluid Mechanics 101. June 4, 2020.

[8] PhD, Everton Gomede. "The Fourier Transform and Its Application in Machine Learning." The Modern Scientist, 4 Dec. 2023

[9] Cumpsty, N. A. Compressor Aerodynamics. New York: Wiley, 1989

[10] Hill, Philip G, and Carl R Peterson. Mechanics and Thermodynamics of Propulsion. Reading, Mass., Addison-Wesley Longman, 2010

[11] Byron W Brown and Guy R Bradshaw, Design and performance of family of diffusing scrolls with mixed-flow impeller and vaneless diffuser, US Government Printing Office, 1950

[12] Ellis, G. O. "A Study of Induced Vorticity in Centrifugal Compressors." Journal of Engineering for Power, vol. 86, no. 1, 1 Jan. 1964, pp. 63–73, https://doi.org/10.1115/1.3675420. Accessed 20 Oct. 2021.

[13] T. Turunen-Saaresti, A. Reunanen, & J. Larjola. Computational and experimental study of pinch on the performance of a vaneless diffuser in a centrifugal compressor. Journal of Thermal Science, 15(4):306–313, Dec. 2006. ISSN 1003-2169. doi: 10.1007/s11630-006-0306-1.

[14] Senoo, Y., Kinoshita, Y., and Ishida, M. (1977). Asymmetric Flow in Vaneless Diffusers of Centrifugal Blowers. Journal of Fluids Engineering, 99(1):104–111.

[15] Fujisawa N., Tajima K., Miida H., and Ohta Y. (2020). Generation mechanism of diffuser stall in a centrifugal compressor with vaneless diffuser. Journal of the Global Power and Propulsion Society. 4: 190–201. https://doi.org/10.33737/jgpps/128974

[16] Senoo Y., Kinoshita Y., Influence of inlet flow conditions and geometries of centrifugal vaneless diffusers on critical flow angle for reverse flow. Journal of Fluids Engineering, 1977, 99(1): 98–102.

[17] Ljevar S., De Lange H., Van Steenhoven A., Two-dimensional rotating stall analysis in a wide vaneless diffuser. International Journal of Rotating Machinery, 2006, Article ID: 56420

[18] Zhang, Qian, et al. "Effect of Vaneless Diffuser Shape on Performance of Centrifugal Compressor." Applied Sciences, vol. 10, no. 6, 12 Mar. 2020, pp. 1936–1936, https://doi.org/10.3390/app10061936

[19] Guadagni, Giachi, Fusi, Farina. (2020). Flow stability in a wide vaneless diffuser. Applications in Engineering Science, 4, 100025